Computers in Biology and Medicine 114 (2019) 103432

Contents lists available at ScienceDirect

Computers in Biology and Medicine

journal homepage: http://www.elsevier.com/locate/compbiomed

Self-adaptive weighted level set evolution based on local intensity difference for parotid ducts segmentation

Xuan Deng [a,1], Tianjun Lan [c,1], Zhifeng Chen [b], Minghui Zhang [a], Qian Tao [c], Zhentai Lu [a,*]

[a] School of Biomedical Engineering, Southern Medical University, Guangzhou, China
[b] Department of Stomatology, Nanfang Hospital, Southern Medical University, Guangzhou, China
[c] Department of Oral and Maxillofacial Surgery, Guanghua School of Stomatology, Hospital of Stomatology, Sun Yat-sen University, Guangdong Provincial Key Laboratory of Stomatology, Guangzhou, China

ARTICLE INFO

Keywords:
PDs segmentation
Local mean difference
Local variance difference
Self-adaptive weighted
Level set method

ABSTRACT

Background: Parotid ducts (PDs) play an important role in the diagnosis and treatment of parotid lesions. Segmentation of PDs from Cone beam computed tomography (CBCT) images has a significant impact to the pathological analysis of the parotid gland. Although level set methods (LSMs) have achieved considerable success in medical imaging segmentation, it is still a challenging task for existing LSMs to precisely and self-adaptively segment PDs from parotid duct (PD) images with both noise, intensity inhomogeneity, and vague boundary. In this paper, we propose a novel Self-adaptive Weighted level set method via Local intensity Difference (SWLD) to comprehensively solve the above issues.

Method: Firstly, a new adaptive weighted operator based on local intensity variance difference has been proposed to overcome the limitations of previous LSMs that are sensitive to parameters, which achieves the aim of automatic segmentation. Secondly, we introduce local intensity mean difference into the energy function to improve the curve evolution efficiency. Thirdly, we eliminate the effects of intensity inhomogeneity, noise, and boundary blur in the parotid image through a local similarity factor with two different neighborhood sizes.

Results: Using the same dataset, segmentation of PDs is performed using the proposed SWLD algorithm and existing LSM algorithms. The mean Dice score for the proposed algorithm is 91.3%, and the corresponding mean Hausdorff distance (HD) is 1.746.

Conclusion: Experimental results demonstrate that the proposed algorithm is superior to many existing level set segmentation algorithms, and it can accurately and automatically segment the PDs even in complex gradient boundaries.

1. Introduction

The diameter, size and angle of the parotid duct are all related to the clinic and can be indicative of pathological processes, accurate division of parotid duct is the precondition to study its morphological features, which has a prominent role in the diagnosis and treatment of parotid gland disease [1–3]. However, due to the bad factors in clinical image data caused by atomic scattering and high attenuation, such as noise, intensity inhomogeneity and blurred border, the segmentation results of traditional segmentation methods [4–9] are discontinuous, unsmooth and fail to approach the real boundary of the image. As shown in Fig. 1, Fig. 1(a) is a result of CBCT examination within 5 min after the patient's left parotid gland injecting with contrast agent, Fig. 1(b) shows the noise generated by severe attenuation of X-rays passing through highly attenuated objects (metal materials, etc.). Fig. 1(c) is the corresponding RadiAnt software reconstruction result. It is apparent from the area indicated by the blue arrow in Fig. 1(a) that there are blurred edges of the catheter, heterogeneous intensity and a large number of small particle targets in the image, which pose great challenges to the actual segmentation.

LSMs are widely used in image segmentation due to its superior performance in handing topological changes and smooth behavior [10–13], especially in the fields of medicine and artificial intelligence [14,15]. Existing LSM can be generally grouped into two parts:

* Corresponding author.
E-mail address: luzhentai@163.com (Z. Lu).
[1] Xuan Deng and Tianjun Lan contributed equally to this work.

https://doi.org/10.1016/j.compbiomed.2019.103432
Received 28 June 2019; Received in revised form 3 September 2019; Accepted 3 September 2019
Available online 4 September 2019

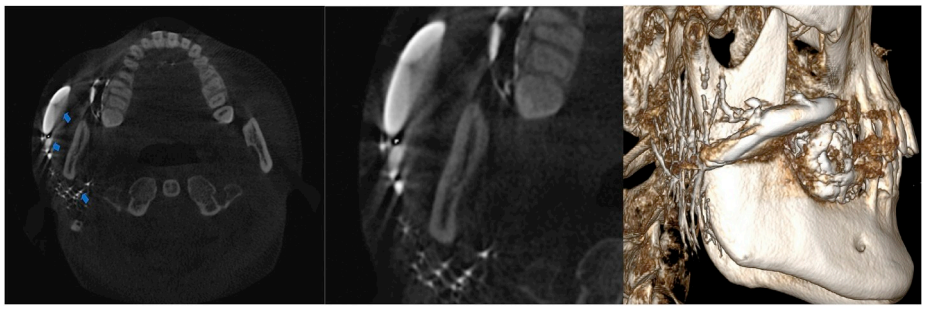

Fig. 1. Parotid gland images. (a) The CBCT scan result of parotid duct. (b) Metal strip noise. (c) The RadiAnt Software reconstruction result of the parotid duct.

edge-based methods [16–22] and region-based methods [23–29]. Edge-based methods utilize the gradient information to separate the desired object from its background, while they are more sensitive to the boundaries presenting weak gradient magnitude. Region-based models rely on a certain region descriptor to guide the motion of the active contour. For example, the classical region-based model proposed by Chan and Vese [5] (CV model) utilizes the statistical information to conduct the curve evolution, and the model is initially proposed based on the assumption that the image is a piecewise constant function to solve the Mumford-Shah [30–33] problem. Although CV model has several advantages (including the less sensitivity to noise and boundaries) over the edge-based methods, the method could not accurately segment the detailed images of the PDs due to only considering the intensity level information of the global region.

In order to overcome the shortcoming that the global region cannot express the image information well, Li et al. [7] proposed the local binary fitting active contour model (LBF) based on local area by introducing the local information of image in energy functional, which can be effective in processing images with intensity inhomogeneity. However, the model is sensitive to parameters and can't converge to the correct edge of the image adaptively when processing noise and boundary blur images. Niu et al. [34] proposed the Region-based model via Local Similarity Factor (RLSF) model with strong robustness to noise, while this method does not solve the problem of parameter sensitivity, and it also has flaws in processing images with rich intensity levels and weak gradient edges.

Based on above analysis, we design a novel level set method to improve the performance of PDs segmentation. In this work, we make three main contributions: first, the difference between the internal and external intensity mean values of the contour is added to the energy function, which accelerates the curve convergence. Second, the neighborhood mean value operator is used to calculate the local neighborhood intensity mean value. While expressing the local image information, the image is smoothed to some extent, eliminating the influence of partial noise and intensity unevenness on the segmentation result. Third, the homogeneity difference between internal and external local neighborhoods substitute for λ_1 and λ_2 in the LBF model as the control items of internal and external local energy parameter values, which solves the problem that the model is sensitive to parameters, and improves the evolution efficiency of the curve.

2. Materials and methods

2.1. Image data

We employ a collection of PDs images from 53 different patients acquired at the Hospital of the stomatology of the Sun Yat-sen University. For every patient, the CBCT (DCT Pro, EWOO, Korea) images were taken within 5 min after introducing the iodinated oil into the orifice of the parotid duct. The following imaging parameters were used: 5 mA, 90–95 kV; field of vision, 16 cm × 16 cm × 10 cm; slice thickness, 0.4 mm; Axial plane resolution, $0.3 \times 0.3\,mm^2$. We invited an experienced physician manually delineated the PDs (including the unilateral and bilateral PDs) on CBCT images.

2.2. Principle of the proposed SWLD method

Motivated by the strengths of RLSF model in noise image segmentation, we introduces a local similarity factor (LSF) with two different neighborhood sizes to reduce the effects of noise and preserve image details. In fact, for a given image $I(x)$ $(x \in \Omega)$, Ω is the image domain, the intensity of each pixel is similar to the intensity of the corresponding neighborhood. In the algorithm of this paper, the neighborhood corresponding to each center point consists of two parts: a square neighborhood of size $p \times p$ and a circular neighborhood of radius r (general$r > p$). The LSF is defined pixel-by-pixel within the image I as:

$$LSF(x, LM) = \int_{(y \in N_x) \neq x} \frac{|I(y) - LM|^2}{d(x, y)} dy \tag{1}$$

Where N_x is the local square neighborhood of the center point x, and y is the pixel point in the local neighborhood, $d(x, y)$ denotes the Euclidean distance between them. Obviously, the weight of the pixel in the neighborhood is determined by its corresponding to the Euclidean distance from the center point, which controls the balance between reducing the noise effect and retaining the image details. LM denotes the local neighborhood intensity mean value of the center point x, it is calculated as:

$$LM(x) = \frac{\int_\Omega R(x, y) I(y) dy}{\int_\Omega R(x, y) dy} \tag{2}$$

With the weight factor of the circular neighborhood $R(x, y)$ defined as:

$$R(x, y) = \begin{cases} \frac{1}{N} & d(x, y) \leq 1 \\ 0 & otherwise \end{cases} \tag{3}$$

N is the number of pixel points in the local circular neighborhood of the center point x (including the x point), r is the radius of the local circular neighborhood. It can be seen from Eq. (3) that the smoothing operator is used to calculate the circular neighborhood weight value, therefore the effects of noise and intensity inhomogeneity are eliminated to some extent.

In addition, in order to increase the performance of the proposed method in the efficiency of segmentation and achieve the goal that the weights can be changed adaptively during the segmentation process, we introduce two new concepts of local intensity information: *the mean difference* (LMD) and *the variance difference* (LVD). The LMD reflect the intensity divergence between the inner and outer contours. When the value of LMD is large, the evolution curve contour will be close to the edge of the real targets, and the energy is approached to the minimum value. Therefore, we use it as part of the energy term to speed up the energy convergence of the curve. On the other hand, the LVD represents the homogeneity divergence between the inner and outer local region,

Table 1
The proposed SWLD algorithm.

Input:Image*I*and model parameters $\mu\nu\gamma\varepsilon,\Delta t,r$and p

1. Initialize LSF $\varphi^{(0)}$;
2. Calculate the Euclidean distance$d(x,y)$ and the circular neighborhood weighting factor $R(x,y)$via Eq. (3);

for $t = 1, 2, \ldots, Iter$ ***do***

3. Calculate the local intensity mean value$LM_1(x)$and$LM_2(x)$ according to Eq. (4);
4. Calculate the local similarity factor (LSF):

$$LSF(x, LM_1(x)) = \int_{(y\in N_x)\neq x} \frac{|I(y) - LM_1(x)|^2}{d(x,y)} dy,\ LSF(x, LM_2(x)) = \int_{(y\in N_x)\neq x} \frac{|I(y) - LM_2(x)|^2}{d(x,y)} dy;$$

5. Calculate the local mean difference ε^{LMD} and the local variance difference α_1 and $\alpha_2$via Eq. (7) and Eq. (8);
6. Calculate the evolution equation:

$$\frac{\partial\varphi(x)}{\partial t} = \delta_\varepsilon(\varphi(x))[\alpha_2 LSF(x, LM_2(x)) - \alpha_1 LSF(x, LM_1(x)) + \varepsilon^{LMD}]$$

$$+\mu\left(\nabla^2\varphi - div\left(\frac{\nabla\varphi}{|\nabla\varphi|}\right)\right) + \nu\delta(\varphi)div\left(\frac{\nabla\varphi}{|\nabla\varphi|}\right)$$

7. Update the LSF: $\varphi^{(t+1)} = \varphi^{(t)} + \frac{\partial\varphi}{\partial t}\Delta t$;

end for

Output: Level set function $\varphi^{(Iter)}$after iteration *Iter* times

which can change constantly according to the gray uniformity of the local neighborhood and automatically adjust the path and direction of the curve motion in the curve evolution process. We replace the parameters λ_1 and λ_2 in the LBF model with the local variance difference α_1 and α_2 as the weight control term of the local energy parameter values inside and outside the contour. The local neighborhood intensity mean value inside $LM_1(x)$ and outside $LM_2(x)$ the contour of the pixel can be formulated as:

Table 2
Parameters used in the LMD part, the LVD part, the LSF part and the SWLD part. The symbol ν, μ,ε,Δt are parameters of the penalty term and length constraint term, and their values do not change.

SYMBOL	Quantity	LMD part	LVD part	LSF part	SWLD part
ν	Length term constant	0.5×255^2	0.5×255^2	0.5×255^2	0.5×255^2
μ	Regularization constant	1.0	1.0	1.0	1.0
ε	Dirac constant	1.0	1.0	1.0	1.0
Δt	Time-step	0.1	0.1	0.1	0.1
γ	negative constant	–	−1.0	−1.0	−1.0
λ_1	Internal energy term coefficient	–	1.0	–	–
λ_2	External energy term coefficient	–	1.0	–	–
p	The rectangular neighborhood window	5×5	5×5	–	5×5
r	the circular neighborhood radius	7.0	7.0	–	7.0

Table 3
Comparison of different parts on Dice metric and HD for parotid gland segmentation on 28 unilateral images and 25 bilateral images.

Methods	The unilateral PD 28 cases		The bilateral PD 25 cases	
	Dice	HD(mm)	Dice	HD(mm)
LMD part	0.704	77.944	0.802	31.330
LVD part	0.765	41.035	0.561	114.015
LSF part	0.559	30.294	0.379	81.181
SWLD part	**0.916**	**1.845**	**0.909**	**1.634**

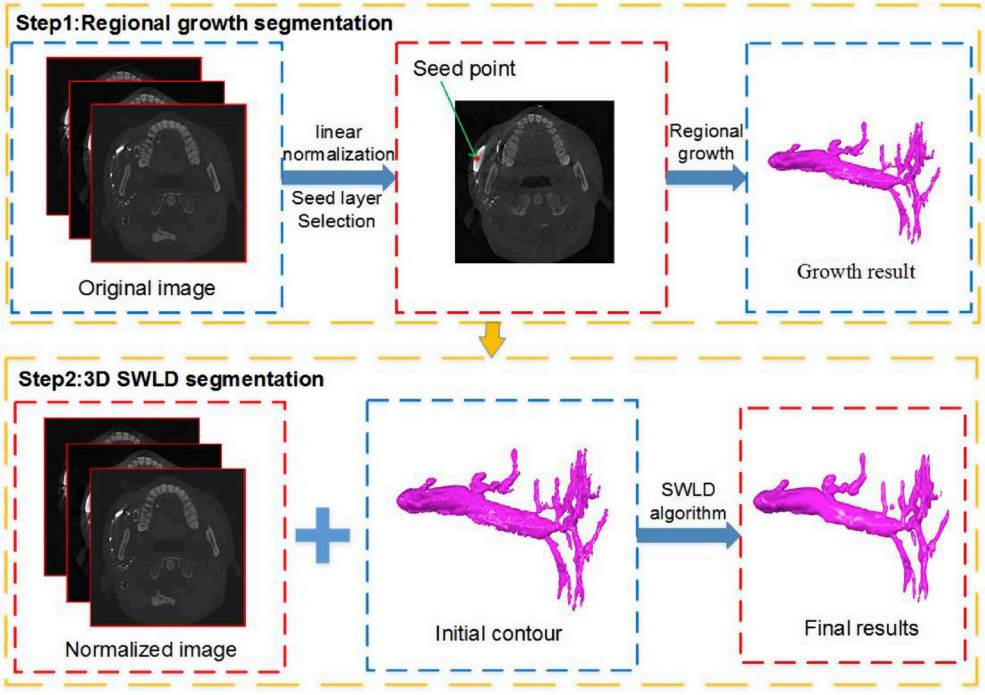

Fig. 2. Flow chart of 3D parotid gland segmentation algorithm.

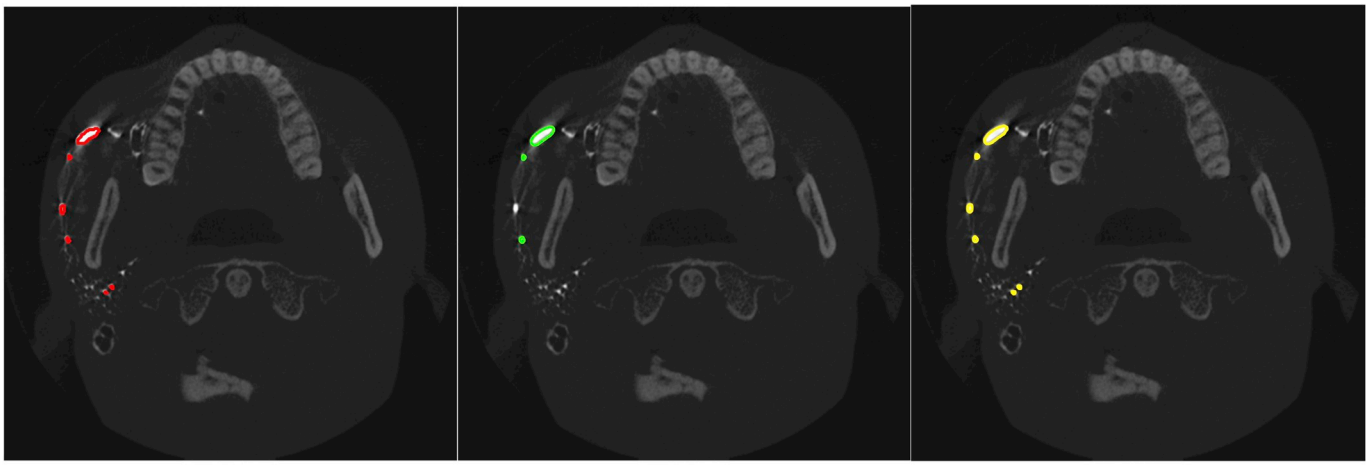

(a) (b) (c)

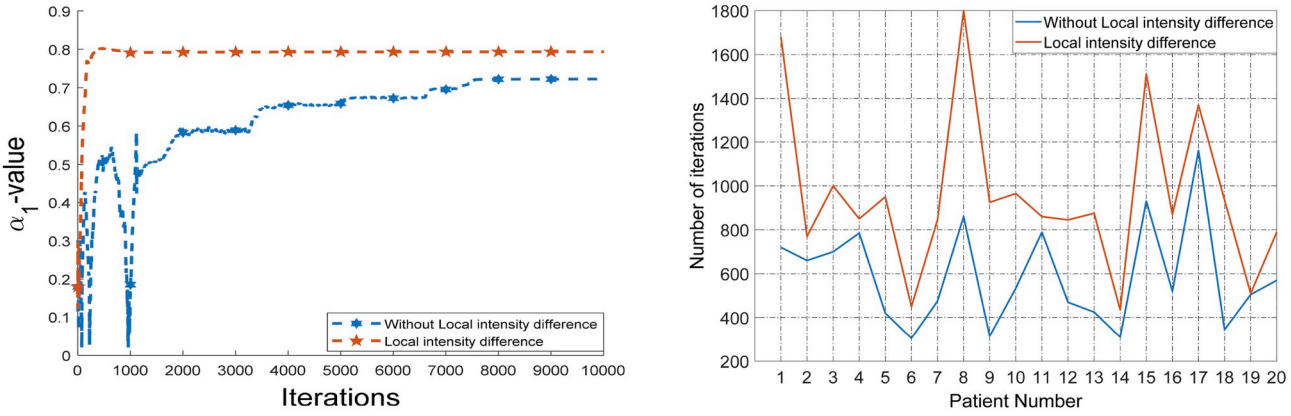

(d) (e)

Fig. 3. An example showing the performance of the SWLD method with or the one without LMD. (a) Original image with ground truth (red). (b) The result of SWLD without LVD (green). (c) The result of SWLD with LVD (yellow). (d) The LVD value comparison between SWLD with LMD and without LMD. (e) The number of iterations required for the convergence of LVD value in the process of segmentation of 20 images randomly extracted from dataset.

$$\begin{cases} LM_1(x) = \dfrac{\int_\Omega R(x,y)I(y)H_\varepsilon(\varphi(y))dy}{\int_\Omega R(x,y)H_\varepsilon(\varphi(y))dy} \\ LM_2(x) = \dfrac{\int_\Omega R(x,y)I(y)(1-H_\varepsilon(\varphi(y)))dy}{\int_\Omega R(x,y)(1-H_\varepsilon(\varphi(y)))dy} \end{cases} \tag{4}$$

$H_\varepsilon(\varphi(x))$ and $\delta_\varepsilon(\varphi(x))$ are the Heaviside function and the Dirac function, which guarantee the smoothness of curves and ensure that the level set function after each curve evolution is a symbolic distance function [35].

$$H_\varepsilon(\varphi(x)) = \frac{1}{2}\left(1+\frac{2}{\pi}\arctan\left(\frac{\varphi(x)}{\varepsilon}\right)\right) \tag{5}$$

$$\delta_\varepsilon(\varphi(x)) = \frac{1}{\pi}\frac{\varepsilon}{\varepsilon^2+(\varphi(x))^2} \tag{6}$$

Then the corresponding local mean difference ε^{LMD} and local variance difference α_1 and α_2 are calculated as:

$$\varepsilon^{LMD} = \gamma\int_\Omega |LM_1(x)-LM_2(x)|^2 dx \tag{7}$$

$$\begin{cases} \alpha_1 = \displaystyle\int_\Omega \frac{\left|\Gamma^2(LM_1(x))-\Gamma^2(LM_2(x))\right|^{\frac{1}{2}}}{\Gamma(LM_2(x))}dx \\ \alpha_2 = \displaystyle\int_\Omega \frac{\left|\Gamma^2(LM_1(x))-\Gamma^2(LM_2(x))\right|^{\frac{1}{2}}}{\Gamma(LM_1(x))}dx \end{cases} \tag{8}$$

Where γ is a negative constant, $\Gamma(Y)$ represents the standard deviation of Y. The internal uniformity of the curve can be considered lower than the external uniformity when the local intensity variance inside the evolution curve is larger than the external ($\Gamma(LM_1(x))>\Gamma(LM_2(x))$). At this time, the weight of the internal energy of the curve should be increased to lower its impact on the curve evolution; conversely, increase the proportion of external energy of the curve. The energy function takes the minimum value and the algorithm obtains the optimal or approximate optimal solution when the homogeneity difference between the two is small enough. In summary, the total energy functional of the proposed

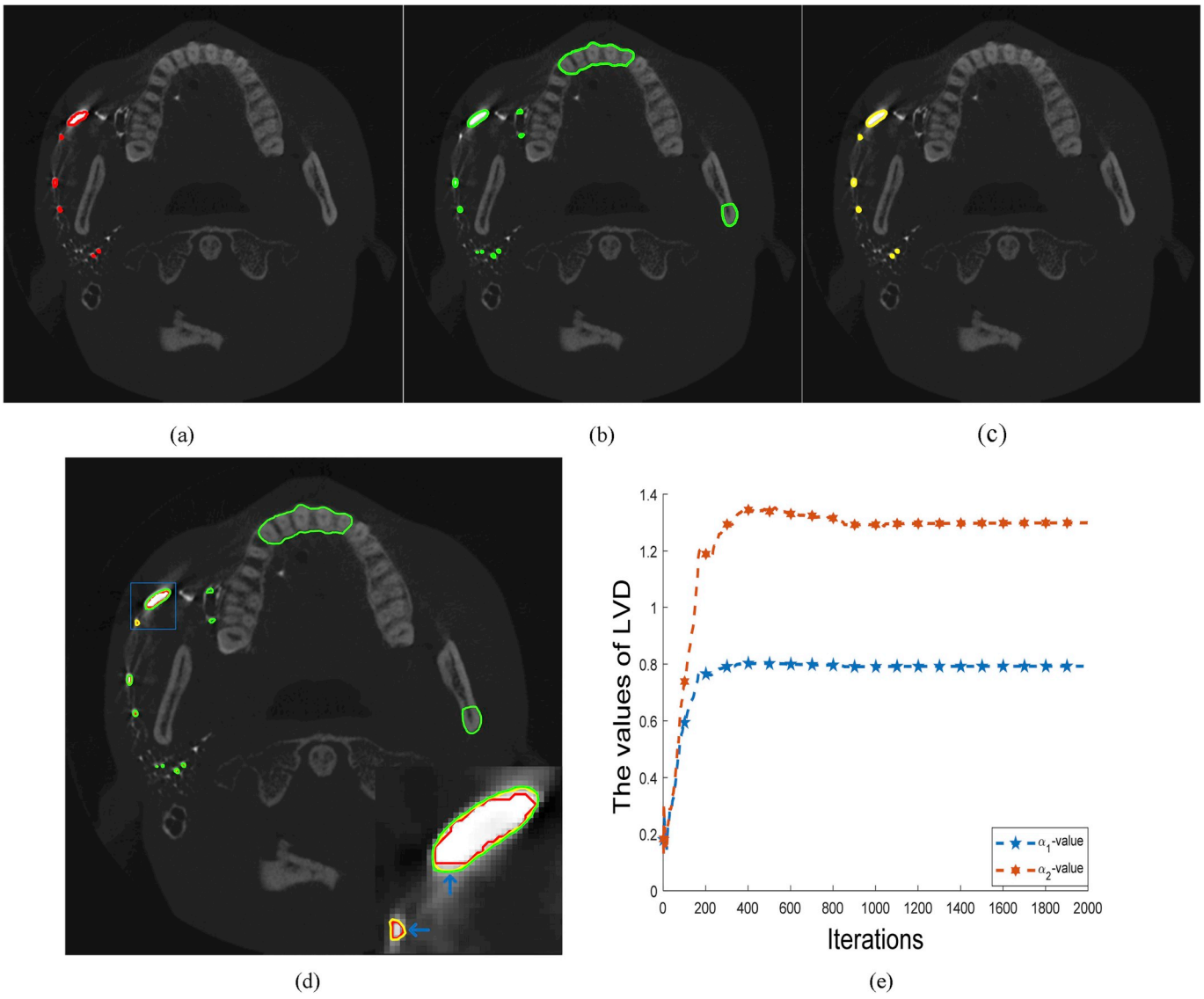

Fig. 4. An example showing the performance of the SWLD method with or the one without LVD. (a) Original image with ground truth (red). (b) The result of SWLD without LVD (green). (c) The result of SWLD with LVD (yellow). (d) The overlapping image of (a), (b) and (c). (e) the LVD variants value of SWLD with LVD.

SWLD model is defined by:

$$
\begin{aligned}
E^{SWLD} &= \alpha_1 \int_\Omega LSF(x, LM_1(x))H_\varepsilon(\varphi(x))dx \\
&+\alpha_2 \int_\Omega LSF(x, LM_2(x))(1 - H_\varepsilon(\varphi(x)))dx \qquad + \varepsilon^{LMD} \\
&+\mu \int_\Omega \frac{1}{2}(|\nabla\varphi(x)| - 1)^2 dx + \nu \int_\Omega |\nabla H_\varepsilon(\varphi(x))|dx \\
&= \alpha_1 \int_\Omega \left(\int_{(y\in N_x)\neq x} \frac{|I(y) - LM_1(x)|}{d(x,y)}^2 dy \right) H_\varepsilon(\varphi(x))dx \\
&+ \alpha_2 \int_\Omega \left(\int_{(y\in N_x)\neq x} \frac{|I(y) - LM_2(x)|}{d(x,y)}^2 dy \right) (1 - H_\varepsilon(\varphi(x)))dx \\
&+ \mu \int_\Omega \frac{1}{2}(|\nabla\varphi(x)| - 1)^2 dx + \nu \int_\Omega |\nabla H_\varepsilon(\varphi(x))|dx \\
&+ \gamma \int_\Omega |LM_1(x) - LM_2(x)|^2 dx
\end{aligned} \tag{9}
$$

Where μ and ν are fixed positive parameters, φ is a level set function, the first and second term are the distance penalty term and the evolution curve length constraint mentioned in Ref. [36], respectively. Using the gradient descent method, the total energy functional is minimized to obtain the corresponding curve evolution equation as:

$$
\begin{aligned}
\frac{\partial\varphi(x)}{\partial t} &= \mu\left(\nabla^2\varphi - div\left(\frac{\nabla\varphi}{|\nabla\varphi|}\right)\right) + \nu\delta(\varphi)div\left(\frac{\nabla\varphi}{|\nabla\varphi|}\right) \\
&-\alpha_1\delta_\varepsilon(\varphi(x))LSF(x, LM_1(x)) \\
&-\alpha_2\delta_\varepsilon(\varphi(x))LSF(x, LM_2(x)) \\
&+\delta_\varepsilon(\varphi(x))\varepsilon^{LMD}
\end{aligned} \tag{10}
$$

Where ε^{LMD},α_1 and α_2 are given by Eq. (7) and Eq. (8) respectively, and δ_ε is the Dirac function, given by Eq. (6).

2.3. Algorithm implementation

In the RLSF model, the incompressible two-phase flow algorithm is used to re-initialize the level set to ensure the smoothness of the evolution curve [34]. The algorithm of this paper applies the LBF model, which can also ensure the smoothness of the curve evolution process without re-initialization. The proposed SWLD algorithm is summarized in Table 1. In the 3D parotid gland segmentation, we use the SWLD algorithm to correct the segmentation results of the traditional regional

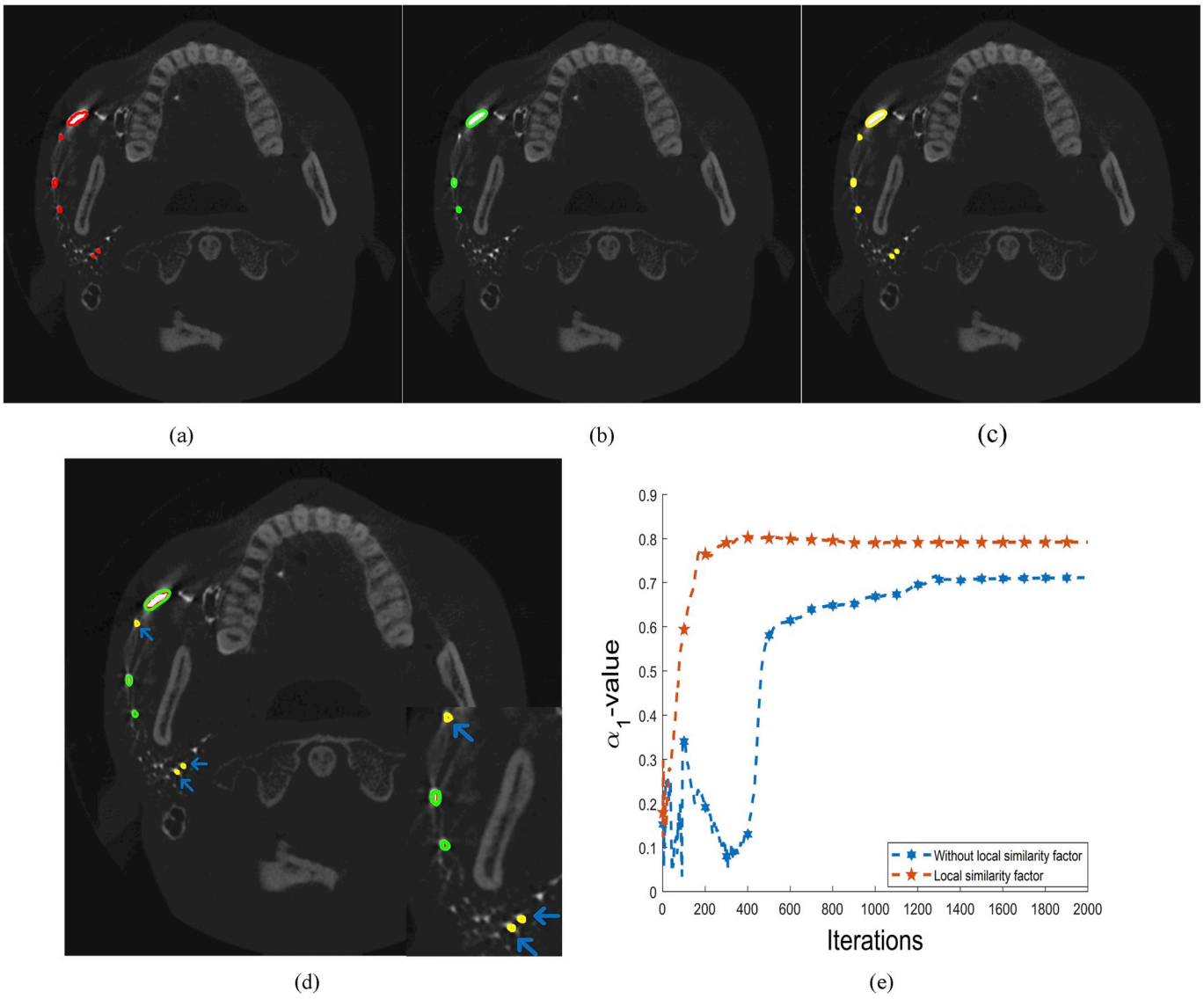

Fig. 5. An example showing the performance of the SWLD method with or the one without LSF. (a) Original image with ground truth (red). (b) The result of SWLD without LSF (green). (c) The result of SWLD with LSF (yellow). (d) The overlapping image of (a), (b) and (c). (e) The LVD variants value of SWLD with LSF.

growth segmentation method according to the local intensity difference of the image and its spatial structure information, Fig. 2 is the flow chart of the 3D algorithm. In step1, the seed layer and the corresponding seed point are first selected from the original image to complete the region growth, and the preliminary segmentation result is obtained. In step 2, it is used as the initial contour of the three-dimensional SWLD algorithm, and finally an accurate three-dimensional segmentation result is obtained.

3. Experiments and results

In the case of CBCT parotid data, linear normalization is performed slice by slice according to the intensity information without changing image size. We performed two-dimensional and three-dimensional PDs segmentation experiments on these data in order to demonstrate the performance of the proposed algorithm. The size of most parotid images is 500×500, and only 5 cases with the size of 400×400 in the unilateral PDs images.

To show an improvement in the feasibility and robustness of the SWLD algorithm, we further performed a segmentation experiment on both the unilateral and bilateral parotid duct images, and compared the SWLD models with the CV model, LBF model and RLSF model. The experiments presented in this section executed on a PC with Intel(R) Core (TM) 3.60 GHz CPU and 8.0 GB RAM using Matlab R2014b software.

3.1. Evaluation metrics

We further assessed the performance of the SWLD model quantitatively by employing two widely used metrics: Dice and Hausdorff Distance (HD) [37]. Let *V(A)* and *V(B)* be the volume of the ground-truth segmentation, $H_1 = \max_{a\in A}(\min_{b\in B} d(a, b))$, $H_2 = \max_{b\in B}(\min_{a\in A} d(a, b))$, and d(a, b) is the Euclidean distance between two points a and b. Dice and HD can be defined as:

$$Dice = \frac{2V(A \cap B)}{V(A) + V(B)} \qquad HD = \max(H_1, H_2) \tag{11}$$

3.2. Quantitative comparison of segmentation results

In this section, we will conduct step-wise comparisons to evaluate the validity of each of the components presented in Section 2. The experiments are divided into four parts, i.e. The LMD part, The LVD part, The LSF part and The SWLD part. The parameter configuration of four parts

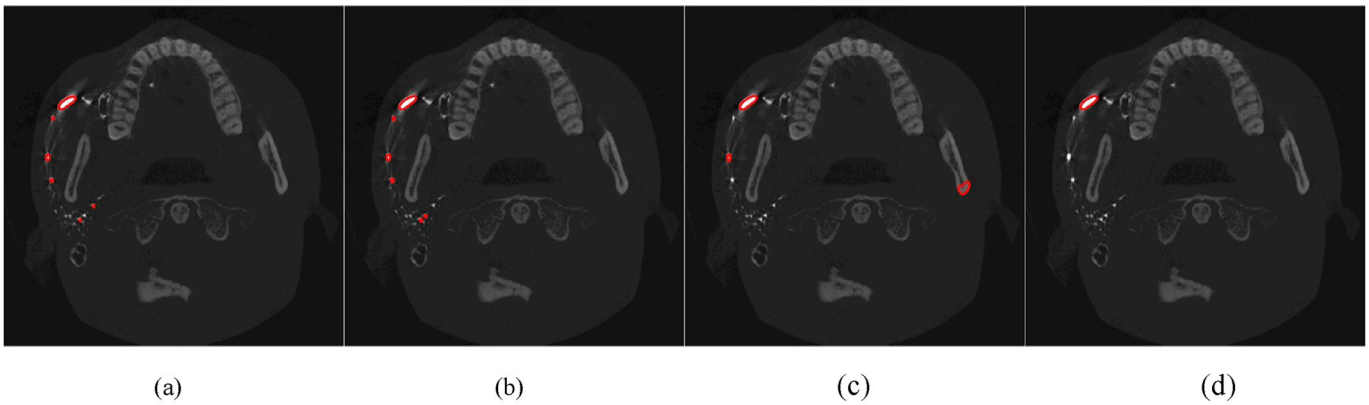

(a) (b) (c) (d)

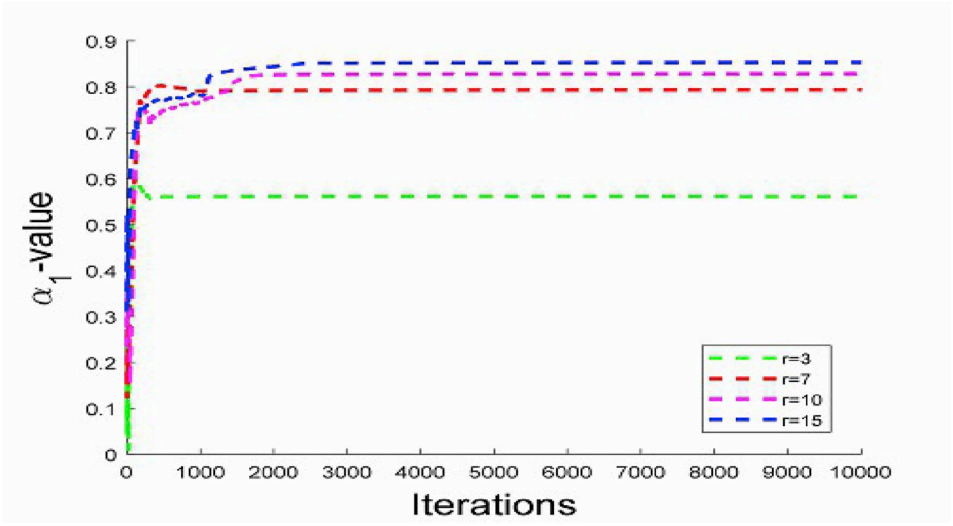

(e)

Fig. 6. (a)–(d) Segmentation results of SWLD with a radius size 3,7,10,15 pixels, respectively (window size $p = 5 \times 5$). (e) The LVD value recorded at each iteration. Remaining parameters were set to $\nu = 0.5*255^2$, $Iter = 10000$, $\gamma = -1.0$, $\mu = 1.0$.

are shown in Table 2. Note that LMD part denotes that SWLD without LMD, LVD part denotes that SWLD without LVD, and LSF part denotes that SWLD without LSF. The comparison results of Dice metric and HD for the PDs segmentation are shown in Table 3. In LMD part, we present a preliminary convergence analysis by comparing the energy function with LMD and the one without LMD to the number of iterations required for the same segmentation effect. The variance difference and local similarity factor are still utilized. In LVD part, the values of λ_1 and λ_2 are set to a fixed positive parameter 1.0 (represent the case without LVD), and the local variance difference α_1 and α_2 replace them as the control term of the local energy weights (represent the case with LVD). Similarly, in LSF part, the energy term uses the energy term of LBF model, but the energy control term still uses LVD and introduces LMD, which means the case without LSF. In SWLD part, all components (including LMD, LVD and LSF) are utilized.

A total of 53 parotid gland images were tested to judge the superiority of each component. Note that the result of the proposed SWLD method yields the highest Dice value of 0.916 and the lowest HD of 1.845 in Table 3. These prove that the overall improvement for the segmentation accuracy brought by simultaneously utilizing our presented LMD, LVD and LSF is much more than that of the individual part. Comparing with the LVD part and LSF part, the LMD part produce more stable segmentation results in terms of the Dice metric. However, it does not perform well in the terms of HD metric with a value of 77.94 for unilateral PD segmentation. Secondly, from the experiment results of the bilateral segmentation, we can see that LVD part does not obtain competitive HD values, but it perform better Dice value than the LSF part. In the LSF part, the SWLD without LSF performs worst in both unilateral and bilateral PD segmentation, which can be inferred that LSF occupies an important position on the motion of the evolutionary curve.

3.3. Qualitative comparison of segmentation results

In this section, we will qualitatively evaluate the performance of the SWLD model by comparing its results with each component in Section 2. Fig. 3 shows in (a) the original PD image with the initial contour (green), (b) and (c) segmentation of the SWLD method without LMD and SWLD with LMD respectively, (d) the LVD variants value. We can see that the segmentation result generated by SWLD without LMD is not very precise in Fig. 3 (b), where some foreground regions are not segmented. Fig. 3 (c) is the segmentation result of SWLD with LMD, where more particle targets are segmented. Besides, Fig. 3 (d) illustrates that SWLD with LMD converges much faster than it without. Fig. 3 (e) shows the number of iterations required when the LVD value converges in the 20 PD images randomly selected from the data set, which also demonstrates that the introduction of LMD can accelerate the convergence of weights of local energy terms. Similarly, Fig. 4(a) is the ground truth, Fig. 4(b) and (c) visually shows the segmentation results of the SWLD method with LVD and it without. Fig. 4 (d) is the overlapping image of the three, It is apparent from the area indicated by the blue arrow that the result of SWLD with LVD is closer to the ground truth. It shows that SWLD can still automatically adjust the value of LVD even on the fuzzy boundary to ensure that the curve approaches the real boundary. In Fig. 4(e), the LVD variants (α_1 and α_2) value of SWLD with LMD converge to 0.75 and 1.3,

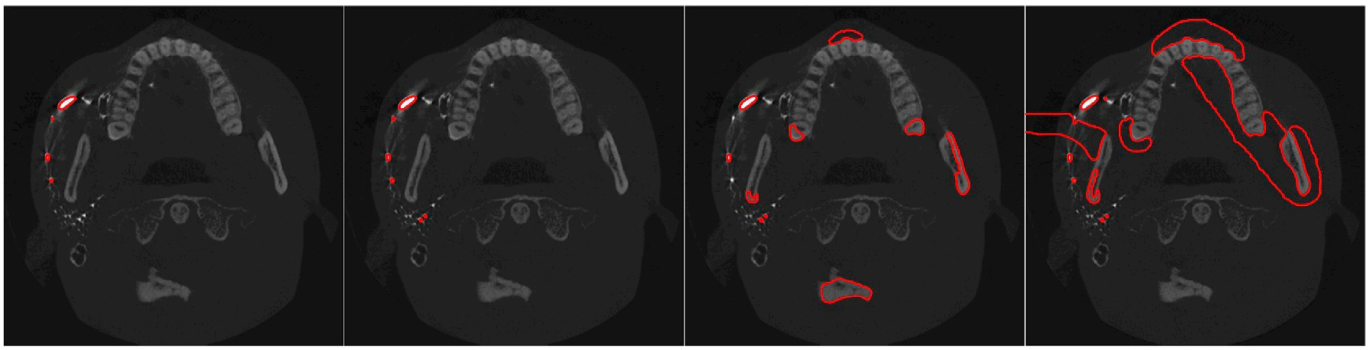

(a) (b) (c) (d)

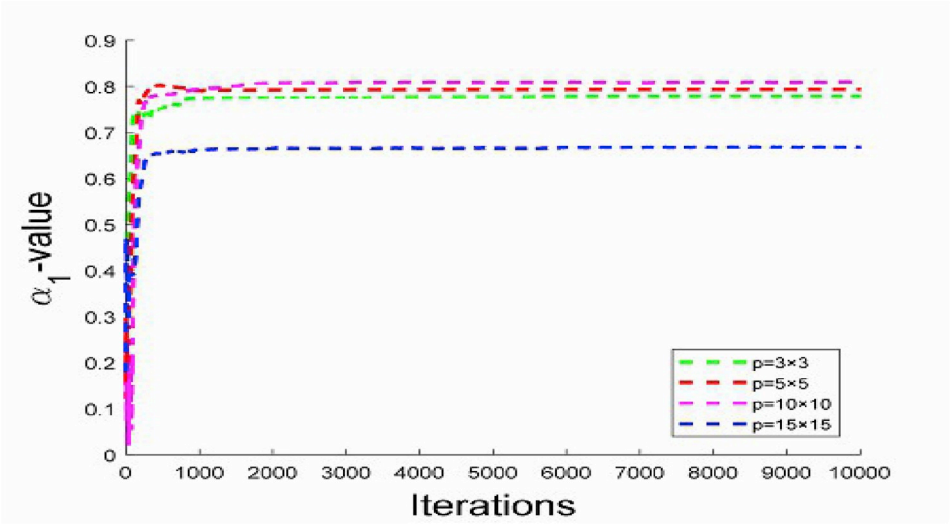

(e)

Fig. 7. (a)–(d) Segmentation results of SWLD with a window size 3×3, 5×5, 10×10, 15×15, respectively (radius size $r = 7.0$). (e) The LVD value recorded at each iteration. Remaining parameters were set to $v = 0.5^{*}255^{2}$, $Iter = 10000$, $\gamma = -1.0$, $\mu = 1.0$.

respectively. However, in the traditional method, these two values are fixedly set to 1.0. Obviously, our method can overcome the influence of parameters on the segmentation effect and automatically adjust the weight values. In addition, it can be observed that from Fig. 5 (d) that there is metal strip noise around the area indicated by the blue arrow, and the SWLD without LSF does not divide the corresponding fine particle target. However, the SWLD with LSF accurately divides it. Fig. 5 (e) shows SWLD with LSF converges much faster than it without, and the LVD value of SWLD without LSF varies unsteadily due to noise during the evolution of the curve, which demonstrates that SWLD improves performance on noise by introducing LSF.

We also evaluated the effects of two parameters (radius and window size) on the LVD's convergence rate. Fig. 6 shows the results of varying the radius while maintaining a constant window size, and Fig. 7 shows the results of varying the window size while maintaining a constant radius. We can observe that choosing a small radius can speed up the curve convergence when the window size is determined. Classically, the window size should be less than radius. From the results, it can be observed that the final evolution curve approaches the target boundary, but depended highly on the selection these parameters. This fact highlights the need of an appropriate parameter selection dependent of the nature of the object to be segmented.

3.4. Comparison with different algorithms

Fig. 8 displays the segmentation results of different algorithms after adjusting to the optimal parameters. Fig. 8(a) is the original image with initial contour (red) and ground truth (green), the image contains many fuzzy boundaries, and there are other weak gradient boundaries and noise. Fig. 8 (b) is the result of CV model segmentation. It can be clearly seen that the evolution curve finally stays on the boundary between two uniform intensity areas, and the target region is not further refined. Fig. 8(c) is the segmentation result of the LBF model. The final evolution curve only stays in part of the target area. Comparing with CV model, it considers the local information of the image and performs relatively well. Nevertheless, it does not segment some noisy target regions. Fig. 8 (d) is the segmentation result of the RLSF model, we can see that most of the target regions more accurately and preserves the boundary details, but here are still a few areas that are not segmented. Fig. 8(e) shows the segmentation result of the SWLD model. It can be observed that even for small particle targets, the final evolution curve can accurately stay at its boundary, which demonstrates that the local neighborhood's intensity difference and LSF is capable of enhancing the ability to manage the intensity inhomogeneity and noise.

Fig. 9 shows the comparison Dice and HD result of the different models evaluated in the 53 parotid gland images. The achieved mean Dice coefficient results from PDs segmentation in other methods are significantly lower than SWLD and reported to be 0.5%, 73.2%, 82.6%, and the corresponding mean value HD are 365.40 mm, 68.54 mm, 29.91 mm, while the SWLD with a Dice of 91.3% and a HD of 1.746 mm. The details can be seen in Table 4, it is not difficult to observe that LBF performs relatively poorly in bilateral parotid segmentation experiments, while RLSF has a better and more stable performance.

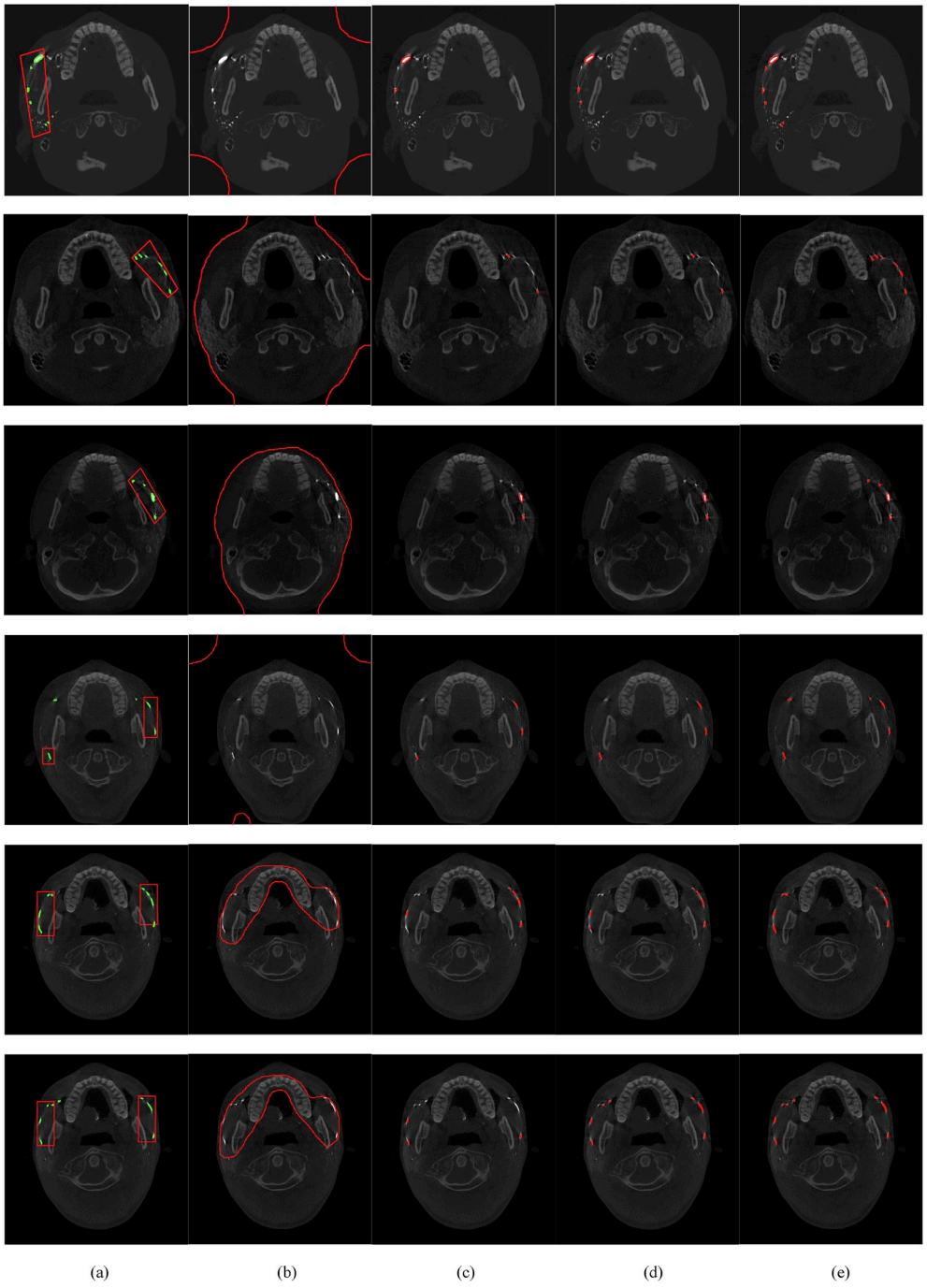

Fig. 8. The comparison with four level set methods on parotid duct segmentation. (a) The unilateral parotid gland images corresponding first to third row, the bilateral parotid gland images corresponding fourth to end row. (b)–(e) Segmentation results of CV model, LBF model, RLSF model and SWLD model, respectively. The initial contour (red) and ground truth (green) are overlapped to the image in the first column, and the final evolution curve is indicated by a red outline. Remaining parameters were set to $v = 0.5*255^2$, $Iter = 2000$, $\gamma = -1.0$, $p = 5 \times 5$, $r = 7.0$, $\mu = 1.0$.

3.5. Three -dimensional parotid image segmentation experiment

In order to show the segmentation results of the parotid gland more intuitively, we performed a segmentation experiment of the three-dimensional parotid gland image. We constructed 3D SWLD using our proposed LMD, LVD and LSF. To construct 3D SWLD, all 2D operations were replaced with their 3D counterparts. Similarly, we obtained a 3D SWLD algorithm. Fig. 10 shows the results of three-dimensional reconstruction after algorithm segmentation. Fig. 10 (a) is the result of region growth, and it is evolved as the initial contour of SWLD algorithm, Fig. 10(b) shows the final result after 20 iterations. Obviously, the result of region growth contains stepped intensity, surface burrs and unevenness, after SWLD algorithm, the surface becomes smooth and continuous, which is due to the introduction of the original image boundary information in the segmentation process. The local intensity difference information corrects the incorrect segmentation points on the complex gradient boundary, and the correct segmentation result is obtained. In terms of the Dice metric and HD, the SWLD method yields mean Dice of 90.4% and mean HD of 2.746 mm, which illustrates that 3D SWLD algorithm can obtain the most competitive segmentation results which are closest to the ground truth.

4. Discussion

Fig. 11 depicts the Dice and HD values of the each single component segmentation method for the whole data set. From the comparing results, one can be see that SWLD achieves the best Dice and HD value. Additionally, it has fewer outliers and more stable than other parts for

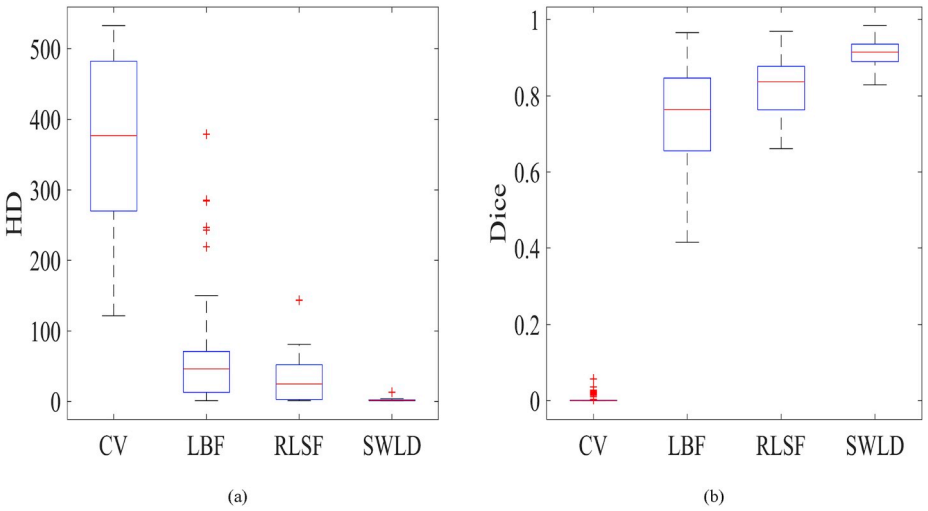

Fig. 9. Boxplot of the Dice and HD calculated for 53 parotid gland images. (a) HD results of four level set methods on parotid duct segmentation, (b) Dice results of four level set methods on parotid duct segmentation.

Table 4
Comparison of different level set methods on Dice metric and HD for parotid gland segmentation on 28 unilateral images and 25 bilateral images.

	The unilateral PD 28 cases		The bilateral PD 25 cases	
	Dice	HD(mm)	Dice	HD(mm)
CV	0.002	459.197	0.009	260.357
LBF	0.766	36.949	0.694	103.93
RLSF	0.846	27.107	0.803	33.055
SWLD	**0.916**	**1.845**	**0.909**	**1.634**

each metric. Note that the most Dice values of LVD part are going to be close to the SWLD part, but there are still five outliers. The overall performance of LMD part is the worst. From these we can infer that the introduction of LVD enhances the stability of the model's segmentation effect on PD images, while LMD improves the segmentation performance of the model.

In Fig. 8, the original image exist metal strip noise and possess boundary ambiguity, facing this challenging, the CV model performs the worst because of only considering the intensity information of the global region during the segmentation process, and does not focus on the local details. Similar to the CV model, Lie et al. [38] proposed a PDE-based (Partial Differential Equation) level set method by introducing a piecewise constant level set function, but it also only pays attention to the global intensity information. To overcome this issue, Zhang et al. [39] proposed the LIF (local image fitting) model, which introduces local image fitting (LIF) energy to extract the local image information, but it performs poorly on images with noise and blurred border. Shortly thereafter, Zhi et al. [40] proposed the SDREL (Saliency Driven Region-Edge-based top down Level set method), which solves the boundary leakage problem. However, it is sensitive to the weight parameters of energy terms.

In this paper, we discussed the limitations of traditional active contour model segmentation on PD images, and proposed a novel self-adaptive weighted level set method based on local intensity difference for the disadvantages of intensity inhomogeneity, noise and boundary blur of parotid duct images. The local variance difference is used to adjust the proportion of the internal and external energy of the curve contour, so that the curve can adaptively and accurately converge to the boundary of the target region during the evolution process, which overcomes the problem that the previous model is sensitive to parameters. Moreover, by exploiting the local mean difference as the energy term and the variance difference as the control term, the curve convergence is accelerated and the curve evolution speed and direction can be adaptively adjusted, which allows good segmentation results to be obtained in a few iterations as shown in Fig. 3.

Although this method deliver extraordinary benefits, there are still some limitations. Firstly, similar to most traditional models [13,24], the SWLD model does not solve the problem of sensitivity to the initial contour. Recent works [41,42] proposed solutions to the limitations by using an adaptive scale for each local region. Piovano et al. [41] proposed the Local Statistic based region segmentation (LSBRS) model, which tested a specific scale for every point through a Gaussian window. This method requires pyramid of predefined scales as input, which is sensitivity to user input regarding scale sizes. To overcome the issue, Hoogi et al. [42] proposed the adapative local window for level set segmentation by adaptively estimating the appropriate local window size for each contour point. However, it has poor performance in images with noise and intensity inhomogeneity.

In addition, since the resulting Dice and HD metric depend on the physician's delineation of parotid ducts on CT image, different doctors may have different understandings and interpretations even when they delineate the catheter area with the same image data, so the interobserver variability should be taken into account. Recent works [43] indicates that different physicians have been reported to be on average 90% among five different observers.

In 3D parotid ducts segmentation, the region growing method and 3D SWLD model are applied to segment parotid ducts. From the results in Fig. 10, most of the parotid duct branches can be segmented by using the proposed algorithm, but there are still some defects in the segmentation of some ultrathin catheters.

5. Conclusion

In conclusion, we proposed a novel PD image segmentation method based on a self-adaptive weighted level set active contour model that provides improved performance on noise, weak edges, Intensity Inhomogeneity. The method uses a local similarity factor to guarantee certain noise robustness and then introduces the mean difference and the variance difference to provide outlines of sufficient detail preservation and improve the evolving efficiency. In terms of experiments, we have successfully implemented accurate two-dimensional parotid duct segmentation and extended the algorithm to three-dimensional parotid segmentation, which may provide reference information for clinicians in the diagnosis and treatment of parotid diseases. Comparisons with several representative methods have demonstrated the effectiveness and the performance of the proposed algorithm.

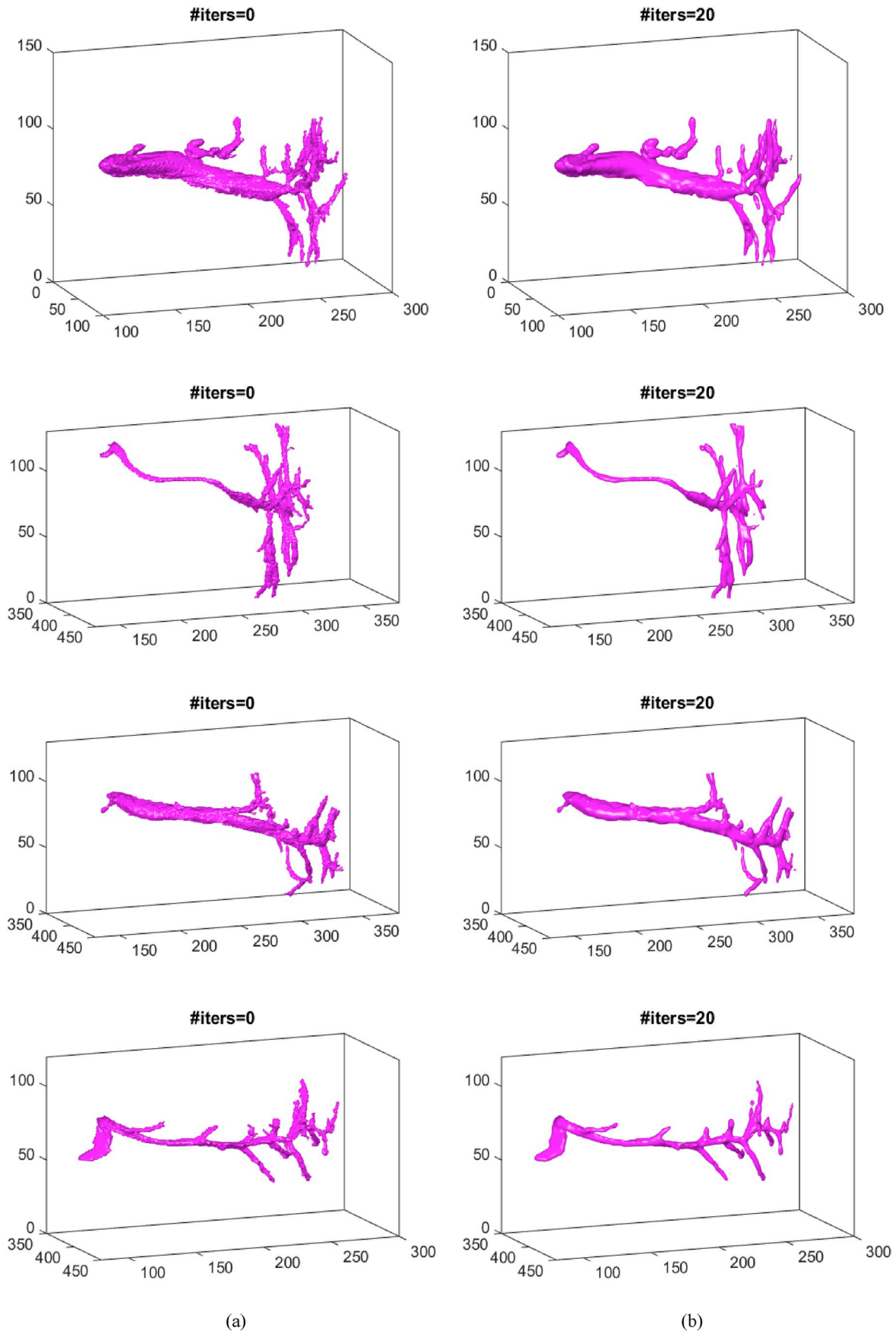

Fig. 10. Results of three-dimensional reconstruction of parotid duct. (a) The initial contour of the three-dimensional SWLD algorithm, (b) The result of the segmentation after 20 iterations. All parameters were set to $v = 0.01 \times 255 \times 255$, $Iter = 20.0$, $\gamma = -1.0$, $p = 5 \times 5 \times 5$, $r = 7.0$, $\mu = 1.0$.

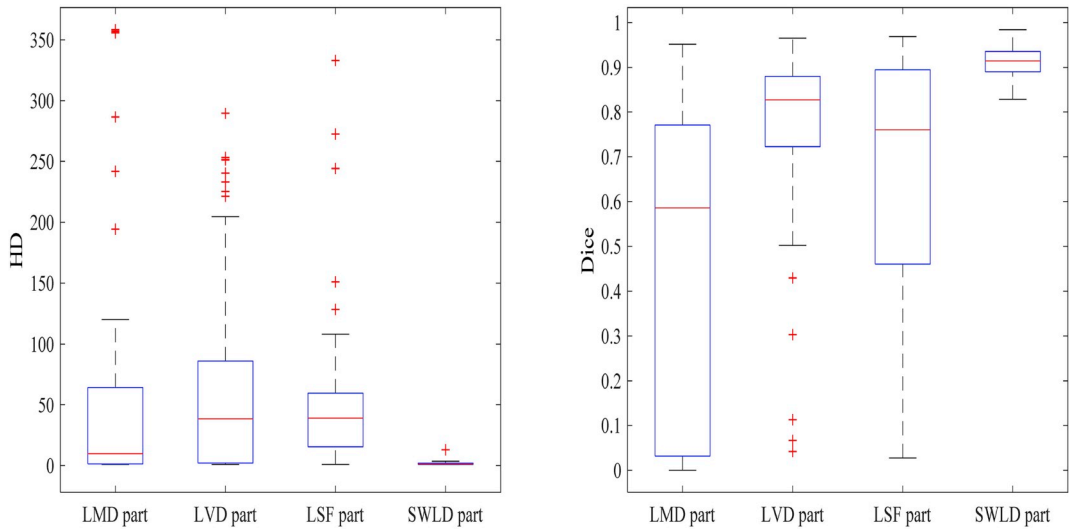

Fig. 11. Boxplot of the Dice and HD calculated for 53 parotid gland images. (a) HD results of four level set methods on parotid duct segmentation, (b) Dice results of four parts on parotid duct segmentation.

Conflicts of interest

None declared.

Acknowledgments

This study supported by Natural Science Foundation of Guangdong Province (NO.2016A030313574, NO.2017A030313891).

Appendix A. Supplementary data

Supplementary data to this article can be found online at https://doi.org/10.1016/j.compbiomed.2019.103432.

References

[1] N.A. Drage, R.F. Wilson, M. McGurk, The genu of the submandibular duct - is the angle significant in salivary gland disease? Dentomaxillofacial Radiol. 31 (1) (2002) 15–18.
[2] T Massoud Horsburgh, The role of salivary duct morphology in the aetiology of sialadenitis: statistical analysis of sialographic features, Int. J. Oral Maxillofac. Surg. 42 (1) (2013) 124–128.
[3] A. Horsburgh, T. Massoud, The salivary ducts of Wharton and Stenson, Analysis of normal variant sialographic morphometry and a historical review, Ann. Anat. 195 (3) (2013) 238–242.
[4] Xua Ni, Narendra Ahujab, Ravi Bansalc, Object segmentation using graph cuts based active contours, Comput. Vis. Image Understand. 107 (3) (2007) 210–224.
[5] T.F. Chan, L. Vese, et al., Active contours without edges, IEEE Trans. Image Process. 10 (2) (2001) 266–277.
[6] V. Caselles, T. Coll, A geometric model for active contours in image processing, Numer. Math. 66 (1) (1993) 1–31.
[7] C. Li, C. Kao, J. Gore, Z. Ding, Minimization of region-scalable fitting energy for image segmentation, IEEE Trans. Image Process. 17 (2008) 1940–1949.
[8] M. Kass, A. Witkin, D. Terzopoulos, Snakes, Active contour models, Int. J. Comput. Vis. 1 (3) (1988) 321–331.
[9] S. Zhu, A. Yuille, Region competition: unifying snakes, region growing, and Bayes/MDL for multiband image segmentation, IEEE Trans. Pattern Anal. Mach. Intell. 18 (1996) 884–900.
[10] Z.Q. Hou, C.Z. Han, Force field analysis snake: an improved parametric active contour model, Pattern Recognit. Lett. 26 (5) (2005) 513–526.
[11] B. Al-Diri, A. Hunter, D. Steel, Snakes, An active contour model for segmenting and measuring retinal vessels, IEEE Trans. Med. Imaging 28 (9) (2009) 1488–1497.
[12] V. Srikrishnan, S. Chaudhuri, Adaptive smoothness based robust active contours, Image Vis Comput. 29 (5) (2011) 317–328.
[13] T.H. Song, V. Sanchez, H. Eldaly, Dual-channel active contour model for megakaryocytic cell segmentation in bone marrow trephine histology images, IEEE (Inst. Electr. Electron. Eng.) Trans. Biomed. Eng. 64 (12) (2017) 2913–2923.
[14] M.E. Lee, S.Y. Park, W.H. Cho, et al., Medical image segmentation using a geometric active contour model based on level set method, in: IEEE Pacific Rim Conference on Communications, Computers & Signal Processing, 2007, pp. 577–580.
[15] Y. Ebrahimdoost, J. Dehmeshki, T.S. Ellis, et al., Medical image segmentation using active contours and a level set model: application to pulmonary embolism (PE) segmentation, in: International Conference on Digital Society, 2010, pp. 269–273.
[16] R. Malladi, J.A. Sethian, B.C. Vemuri, Shape modeling with front propagation: a level set approach, IEEE Trans. Pattern Anal. Mach. Intell. 17 (2) (1995) 158–175.
[17] V. Caselles, R. Kimmel, G. Sapiro, Geodesic active contours, Int. J. Comput. Vis. 22 (1) (1997) 61–79.
[18] A. Vasilevskiy, K. Siddiqi, Flux maximizing geometric flows, IEEE Trans. Pattern Anal. Mach. Intell. 24 (12) (2002) 1565–1578.
[19] N. Badshah, K. Chen, Image selective segmentation under geometrical constraints using an active contour approach, Commun. Comput. Phys. 7 (4) (2010) 759–778.
[20] M. Li, C. He, Y. Zhan, Adaptive level-set evolution without initial contours for image segmentation, J. Electron. Imaging 20 (2011), 023004.
[21] L. Mabood, H. Ali, N. Badshah, K. Chen, G.A. Khan, Active contours textural and inhomogeneous object extraction, Pattern Recognit. 55 (2016) 87–99.
[22] C. Liu, W. Liu, W. Xing, An improved edge-based level set method combining local regional fitting information for noisy image segmentation, Signal Process. 130 (2017) 12–21.
[23] R. Ronfard, Region-based strategies for active contour models, Int. J. Comput. Vis. 13 (2) (1994) 229–251.
[24] L. Vese, T.F. Chan, A multiphase level set framework for image segmentation using the mumford and shah model, Int. J. Comput. Vis. 50 (3) (2002) 271–293.
[25] M. Rousson, R. Deriche, A variational framework for active and adaptative segmentation of vector valued images, IEEE Workshop Motion Video Comput. (2002) 56–61.
[26] T. Brox, D. Cremers, On local region models and a statistical interpretation of the piecewise smooth mumford-shah functional, Int. J. Comput. Vis. 84 (2) (2009) 184–193.
[27] K. Zhang, H. Song, L. Zhang, Active contours driven by local image fitting energy, Pattern Recognit. 43 (4) (2010) 1199–1206.
[28] V. Estellers, D. Zosso, S. Osher, et al., Efficient algorithm for level set method preserving distance function, IEEE Trans. Image Process. 21 (12) (2012) 4722–4734.
[29] Y. Wang, S. Xiang, C. Pan, L. Wang, G. Meng, Level set evolution with locally linear classification for image segmentation, Pattern Recognit. 46 (6) (2013) 1734–1746.
[30] D. Mumford, J. Shah, Optimal approximations by piecewise smooth functions and associated variational problems, Commun. Pure Appl. Math. 42 (5) (1989) 577–685.
[31] A. Tsai, A. Yezzi, A.S. Willsky, Curve evolution implementation of the mumfordshah functional for image segmentation, denoising, interpolation, and magnification, IEEE Trans. Image Process. 10 (8) (2001) 1169–1186.
[32] S. Gao, T.D. Bui, Image segmentation and selective smoothing by using mumford-shah model, IEEE Trans. Image Process. 14 (10) (2005) 1537–1549.
[33] J. Lie, M. Lysaker, X. Tai, A binary level set model and some applications to Mumford-Shah image segmentation, IEEE Trans. Image Process. 15 (5) (2006) 1171–1181.
[34] S. Niu, Q. Chen, Z. Ji, et al., Robust noise region-based active contour model via local similarity factor for image segmentation, Pattern Recognit. 61 (2017) 104–119.

[35] C.M. Li, C. Xu, C. Gui, Level set evolution without Re-initialization: a new variational formulation, IEEE Comput. Soc. Conf. Comput. Vis. Pattern Recognit. 1 (2005) 430–436.
[36] C.M. Li, J. Gore, Z. Ding, Implicit active contours driven by local binary fitting energy, IEEE Conf. Comput. Vis. Pattern Recognit. 1 (2007) 1–7.
[37] M. Meijs, A. Patel, S. Leemput, et al., Robust segmentation of the full cerebral vasculature in 4D CT of suspected stroke patients, Sci. Rep. 7 (1) (2017) 15622.
[38] J. Lie, M. Lysaker, X.C. Tai, A binary level set model and some application to Mumford–Shah image segmentation, IEEE Trans. Image Process. (2006) 1171–1181.
[39] K. Zhang, H. Song, L. Zhang, Active contours driven by local image fitting en- ergy, Pattern Recognit. 43 (2010) 1199–1206.
[40] X. Zhi, H. Shen, Saliency driven region-e dge-base d top down level set evolution reveals the asynchronous focus in image segmentation, Pattern Recognit. 80 (2018) 241–255.
[41] J. Piovano, T. Papadopoulo, Local Statistic Based Region Segmentation with Automatic Scale Selection, European Confidence intervals approach, 2011, pp. 87–93.
[42] A. Hoogi, C. F Beaulieu, G. M Cunha, et al., Adaptive local window for level set segmentation of CT and MRI liver lesions, Med. Image Anal. 37 (2017) 46–55.
[43] D. Thomson, C. Boylan, T. Liptrot, A. Aitkenhead, et al., Evaluation of an automatic segmentation algorithm for definition of head and neck organs at risk, Radiat. Oncol. 9 (1) (2014) 173.